

Research article

John Mativo*, Kevin Hallinan, Uduak George, Greg Reich and Robin Steininger

Topology optimized thermoelectric generator: a parametric study

<https://doi.org/10.1515/ehs-2021-0002>

Received March 18, 2021; accepted June 27, 2021;

published online July 30, 2021

Abstract: Typical thermoelectric generator legs are brittle which limits their application in vibratory and shear environments. Research is conducted to develop compliant thermoelectric generators (TEGs) capable of converting thermal loads to power, while also supporting shear and vibratory loads. Mathematical structural, thermal, and power conversion models are developed. Topology optimization is employed to tailor the TEG design yield maximal power production while sustaining the applied shear and vibratory loads. As a specific example, results are presented for optimized TEG legs with a void volume fraction of 0.2 that achieve compliance shear displacement of 0.0636 (from a range of 0.0504 to 0.6079). In order to achieve the necessary compliance to support the load, the power reduction is reduced by 20% relative to similarly sized void free TEG legs.

Keywords: multifunctional design; parametric design; power; thermoelectric leg geometry; topology optimization.

Introduction

Waste energy in the form of heat is abundant. Heat emitted from large sources such as engines, furnaces, and kilns; or small forms of heat emissions from computers, kitchen appliances, and the human body, exist but difficult to

capture and recover. Locations where heat rejection is found are normally non-planar surfaces, vibratory environments, or both, making it difficult to use thermoelectric devices typically made of brittle materials. Flexible thermoelectric devices are required to access waste heat in areas with such conditions. The objective function for the thermoelectric unit cell's combined structural and thermal load is maximizing displacement and maximizing heat flow. Such a unit cell can be used in non-planar surfaces, and vibratory environments while generating power. In this paper, we briefly review the history of the thermoelectric generator, its limitations, and propose a method that would allow greater access to waste heat locations for the purpose of converting it into electricity.

Thermoelectric generators made of bismuth telluride (Bi_2Te_3) play an increasing role in the conversion of waste heat into electricity for temperatures of up to 230 °C. But their potential for future use is large. TEGs are unique in that they have no moving parts, are reliable, are silent, and can be operated unattended in hostile, inaccessible environments (Kim et al. 2021; Roeser 1940; Telkes 1947; Yang et al. 2020). These characteristics make TEGs the power provider of choice for deep space expeditions and harsh climate operations using radioactive isotopes as heat sources (Ambrosi et al. 2019; Macklin and Moseley 1990; Rowe and Bhandari 1983; Schmidt and Sutliff 2011). Increasingly, because of their ruggedness, portability, and ready ability to produce electricity, TEGs are being adapted to military and civilian application to power systems in aircraft, cars, and trains (Bell 2008). However, Bi_2Te_3 TEGs are limited by their brittleness. This characteristic poses a unique challenge for employing these devices on non-planar surfaces where they can experience shear loadings or in vibratory environments (Choi, Seo, and Choi 2011; McCarty 2008).

Most of the early research on TEGs focused on the use of metals and metal alloys (Agabaev et al. 1979; Macklin and Moseley 1990; Telkes 1947, 1954). There has been significant research focused on TEG material characterization, performance optimization, and energy conversion (Goldsmid 2016; LeBlanc 2014; Ragupathi et al. 2021; Rowe 2006, 2012; Sutton 1966). Numerous previous efforts have

*Corresponding author: John Mativo, Career and Information Studies, and College of Engineering, University of Georgia, 213 River's Crossing, 850 College Station Rd, 30602-0002, Athens, GA, USA, E-mail: jmativo@uga.edu

Kevin Hallinan, Mechanical and Aerospace Engineering, University of Dayton, Dayton, OH, USA, E-mail: kevin.hallinan@udayton.edu

Uduak George, Mathematics and Statistics, San Diego State University, San Diego, CA, USA, E-mail: ugeorge@sdsu.edu

Greg Reich, Research Scientist, Dayton, OH, USA

Robin Steininger, Product and Development, Tranter, Inc, Wichita, TX, USA, E-mail: robin.mccarty@gmail.com

explored the possibility of improving the figure of merit, which is at the heart of TEG operations in power generation (Kim et al. 2015; Poudeu et al. 2006; Tuley and Simpson 2017). Other research has explored modification of the TEG configuration to improve efficiency in power generation (Crane 2006; DiSalvo 1999; Hashim, Bomphery, and Min 2016; Jaziri et al. 2020).

A TEG research aspect that has not received much attention is the influence of geometric configuration on power generation (Sahin and Yilbas 2013). Some prior research has explored TEG geometry (James 1962; LeBlanc 2014; Thacher 1982) without consideration of the effect of geometry on power generation, current flow, and efficiency (Sahin and Yilbas 2013). Still, several creative ways have been developed to use TEGs on non-planar surfaces. Some report exist on the use of flexible foil substrate technology (Glatz, Muntwyler, and Hierold 2006; Qu, Plötner, and Fischer 2001; Saqr and Musa 2009); others have developed flexible thermopile generator with integral slits to enable flexibility (Shiozaki et al. 2004); and others a plurality of thermoelectric elements (U.S. Patent 2004). In addition, new technologies such as carbon nanotubes (Rowe 2006, 2012); graphene nanoribbons (Goldsmid 2016) and nanofilms (Arora et al. 2017) have been examined as alternatives to the brittle bismuth telluride in order to achieve some measure of compliance.

In spite of its brittleness, the allure of using bismuth telluride and its alloys in energy harvesting is very attractive due to their high-energy conversion efficiency at ambient temperature without requiring any moving parts or cooling systems (Mehta et al. 2012). A previous effort by the authors focused on tailoring the design of a printable TEG for specific structural and thermal loads. However, this prior effort did not account for power generation, and thus did not offer any conclusions about the trade-off associated with creating compliance needed to support shear and vibratory loadings on power generation (Mativo and Hallinan 2017).

Here, the previous effort is extended to account for power generation as well as the possibility of developing a composite TEG comprised of Bi_2Te_3 and a conducting electric polymer.

Physical model

Unit cell design

LeBlanc observes three considerations required for a TEG design; namely physical geometry of the TE material and module geometry, the fill factor which is a ratio of the amount of module surface area occupied by TE material to

overall surface area, and leg size. All three affect in some way the desire for high thermal conductivity and low electrical resistivity (Kim 2010).

The model of a potentially compliant Bi_2Te_3 TEG developed previously by the authors (Mativo and Hallinan 2017) was employed here as the starting point for follow-on research. A **Marlow TG12-6** TEG is used as a baseline (Marlow Industries 2015). Within the footprint for this TEG, a unit cell model is developed as depicted in Figure 2.1. As shown, both compressive and shear mechanical loadings are considered. The bottom surface is considered fixed. A uniform thermal load (heat flux) is applied to the top surface. The bottom surface is connected to a heat sink which is assumed in this study to have a nearly zero thermal resistance. A constant sink temperature on the bottom of the TEG is thus considered. The TEG top and bottom substrates are considered to have strong mechanical strength relative to the TEG legs. They are also assumed to be electrically insulating and thermally conducting from the underside of the substrates that are joined to the legs. These substrate materials are typically alumina-based ceramics (Chen, Meng, and Sun 2012; Kim 2010). The TE legs are attached to the substrate; hence, the need for it to have the mechanical strength to support the legs and interconnects. Although thicker ceramic substrates improve mechanical strength of a TEG, they also result in smaller temperature differences between hot and cold sides of the legs (Chen, Meng, and Sun 2012). This results to reduced power generation. Last of all, the sides are treated as insulated; e.g., there may be other TEGs operating in parallel to the one considered in the unit cell, but they are effectively operating under the same thermal and structural conditions.

In this unit cell, S_1 and S_2 are the domains in which Bi_2Te_3 material can be placed (printed) in order to support both the thermal and structural loads. We leave open the possibility of the thermoelectric material filling these domains fully or partially. The street between the legs is considered perfectly insulated.

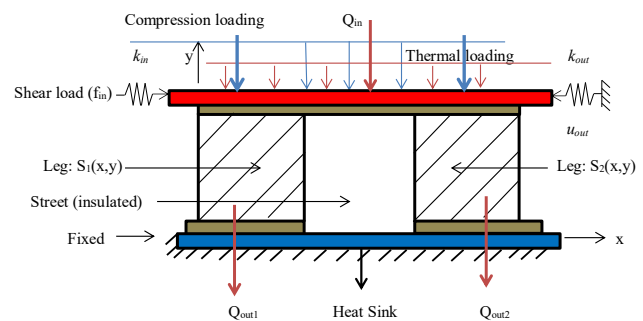


Figure 2.1: Illustrated dimensions of a TEG unit cell subjected to structural and thermal loads.

Compliant mechanisms attain their mobility from the flexibility of their constituents rather than the use of hinges, bearings, and sliders (Bendsoe and Sigmund 2004). The goal of developing a compliant mechanism by appropriately placing TE material within the S_1 and S_2 domains, such as depicted in Figure 2.1, is to maximize displacement (u_{out}) performed on a work-piece modeled by a spring with stiffness k_{out} . For example, a low k_{out} will allow a large displacement. Of particular interest in this study is to allow a horizontal displacement that would accommodate vibrations that could be induced by external cyclical shear loads applied to the TEGs. In this model, it is assumed the material domain is isotropic and the input actuator is a linear strain; hence it is modeled by a spring with a stiffness k_{in} and a force f_{in} . We seek to optimize the shape of the Bi_2Te_3 in the S_i domains in order to provide the necessary compliance, while at the same time maximize power production. The latter is assumed to require constant cross-section.

Assumptions

The physical model considers the possibility of Bi_2Te_3 material filling completely or partially square spaces of height of $1.397\text{e-}3\text{ m}$ and a width of $1.397\text{e-}3\text{ m}$, for both the n and p legs of the TE. The street is considered to be of similar dimensions of a height of $1.397\text{e-}3\text{ m}$ and a width of $1.397\text{e-}3\text{ m}$. The substrates are made of alumina ceramic (Al_2O_3), with a thickness of $5\text{e-}5\text{ m}$. For this substrate material, the electrical conductivity is high (1×10^{12} to $1 \times 10^{13}\ \Omega\text{-m}$), the thermal conductivity is moderate ($30\text{ Wm}^{-1}\text{ K}^{-1}$), the maximum tensile strength is 665 MPa , and the compressive strength is very large ($4,000\text{ MPa}$) (Lee 2013).

The electrical and thermal properties considered for the TEG legs (both n and p) for the Bi_2Te_3 material considered are summarized in Table 2.1 (McCarty 2011; Telkes 1954).

In addition, we leave open the possibility of filling voids in the optimal TE legs with a conducting polymer. The voids expectedly will diminish thermal transport (e.g., increase the thermal resistance and thus the temperature drop along the TE legs).

For this reconfigured TEG, constant and homogenous thermophysical and electrical properties are considered; however volume-weighted properties are employed. Thus,

Table 2.1: Property and values used in the study.

Property	Value	Units
Seebeck coefficient, α_p, α_n	$0.000215, -0.000215$	V K^{-1}
Thermal conductivity, k_p, k_n	1.47	$\text{Wm}^{-1}\text{ K}^{-1}$
Electrical resistivity, ρ_p, ρ_n	$1\text{e-}5$	$\Omega\text{-m}$

for example, the calculation of the reconfigured TEG thermal conductivity given a volume fraction of Bi_2Te_3 of 70% is as described in Eq. (1) below.

$$(k_{\text{BiTe}}) * 0.7 + (k_{\text{void}}) * .3 = k_{\text{new}} \quad (2.1)$$

Though the positive (p -type) and negative (n -type) legs are made of same materials, they have different electron flows. Most good thermoelectric materials are heavily doped semiconductors to achieve high electrical conductivity (Kanimba and Tian 2016). The difference in doping between the n -type and p -type legs induces a greater electron flux in the n -type leg.

Analytical model

Here, we develop a model to analyze displacement, thermal, and energy transport within a designed TEG. As noted previously, this study builds upon the prior work of Mativo and Hallinan (2017), which addressed only the design of TEGs for isolated structural and thermal loadings; and its integrated form, but without consideration of power generation. Here, we also present the model needed to compute power production.

Structural model

Exploring new structure

The exploration for a new compliant structure involves the removal of material to determine if it can support structural loads while maximizing power generation. The effort in the study is geared toward optimizing the holes shown in Figure 3.1 model in order to find the best void structure and develop optimal configurations for different loads for any environment.

Process

Figure 3.2 shows a flowchart that describes the process used to create a unit cell and test it for structural loading.

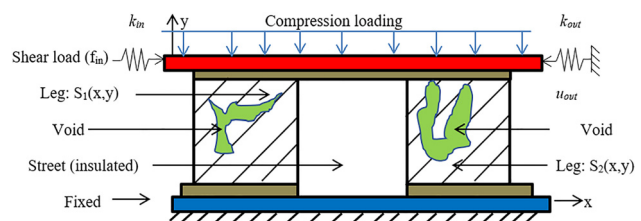


Figure 3.1: Exploring new structure.

The flowchart is a representation of the standard finite element based tool developed by Sigmund (2001). It starts with inputs such as the perimeter area to create the design space. Boundary conditions and loads are prescribed. Input of the design variable is loaded. An even distribution of the design variable is made across the design space. The MATLAB code representation of the model is run as depicted in Figure 3.2.

As shown in the flowchart, also discussed by Liu and Tovar (2014), the iterative process continues with termination occurring when a maximum number of iterations is reached or where the change in material distribution from iteration to iteration is within a specified tolerance; for example, if available material is equal to or less than 0.01. Convergence takes place because the design variable is less than the convergence criteria.

The finite element code makes use of the sparse option in MATLAB. The top left and top right node element numbers are used to insert the element stiffness matrix at the right places in the global matrix. Both nodes and elements are numbered column-wise from left to right. Each node has a designation of two degrees of freedom which are translational for horizontal and vertical of an element node (Figure 3.5). Fixed and free degrees of freedom are

easily entered in the code. The Young's modulus and Poisson's ratio are inputs to the code.

Step one in the process first requires specification of the applied loads, support conditions, volume domain of structure to be constructed, and geometry of the void and solid areas. In developing a design domain, a volume fraction (φ) is defined as a ratio of the object volume versus the available space volume in the material domain (Ω).

Finite elements

The design domain is discretized into elements. A single element is shown (Figure 3.3). Each element has four nodes each with two degrees of freedom (dof); totaling to eight dof. K_e is the element stiffness matrix with a dimension of 8×8 .

A 2D-quad element illustrated in Figure 3.2 has four nodes. Each node has the potential to translate in the x -direction (horizontal) and in the y direction (vertical), when a force is applied to the element. The force applied is proportional to element stiffness and resulting displacement. The relationship is captured in Eq. (3.1).

$$0 = Ku - f \quad (3.1)$$

where the applied force f , is equal to the product of element stiffness K and its displacement u . The stiffness matrix K depends on the vector ρ of the element-wise constant material densities in each element, $e = 1 \dots N$. Therefore, K can be written as

$$K = \sum_{e=1}^N \rho_e^p K_e \quad (3.2)$$

where K_e is the global element stiffness and p is the power which penalizes intermediate densities. A p value of three or greater is preferred (Bendsoe and Sigmund 2004; Liu and Tovar 2014) because a high p level makes it unecological to have intermediate densities in the optimal design. Further, a p value of three or greater will result in obtaining a true "0–1" design for an active volume constraint (Bendsoe and Sigmund 2004).

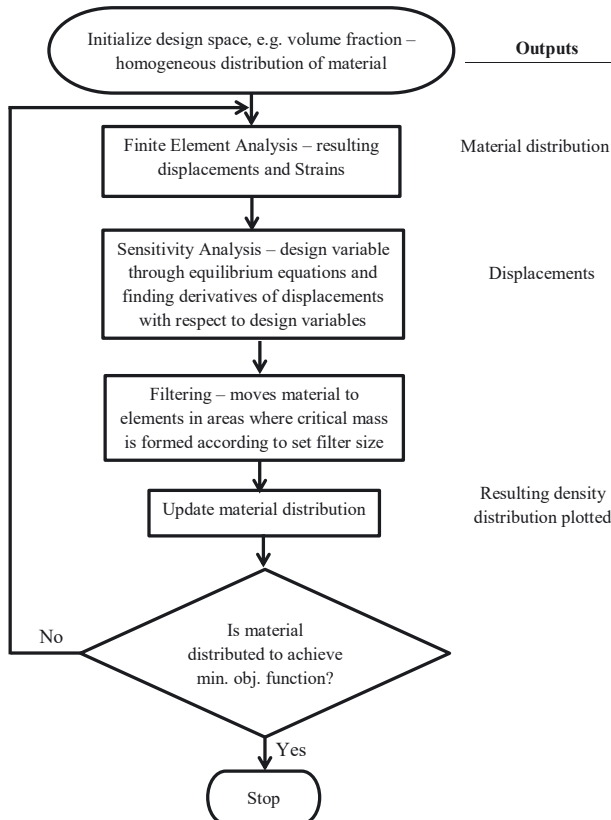


Figure 3.2: Standard topology optimization flow chart.

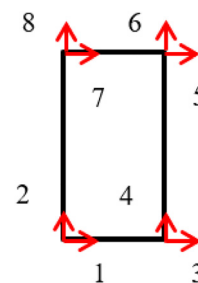


Figure 3.3: Element showing eight dof.

Structural model validation

Bendsoe and Sigmund (2004) discuss how search for the optimal lay-out of structure with a specified region requires applied loads, support conditions, volume of structure to be constructed and location and size of void solid areas. Mativo and Hallinan (2017) use this approach to validate extensively the structural tool. The following three validation examples are provided.

Effects of constraints, and material distribution

A design domain uses support conditions such as fixed elements or nodes that may restrict displacement or transmission of loads. The design function in the design domain is density. The design problem for the fixed domain is formulated as a sizing problem by modifying the stiffness matrix so that it depends continuously on a function which is interpreted as a density of material. Figure 3.4 a and b shown below depicts material distribution that show size, shape, and topology of structures. The volume fraction is symbolized by φ . The difference of the topologies are results of point load applied at two different positions of design domain to support conditions imposed at the bottom of both left and right of the design domain.

Compliant mechanism

Sigmund (2007) explores the design of compliant mechanism using topology optimization. One of the most important objectives in compliant mechanism synthesis is to be able to control ratios between output and input displacements or output and input forces which are described by the geometrical and mechanical advantages respectively. Two examples shown in Figures 3.5 and 3.6, initially presented in Bendsoe and Sigmund (2004), were replicated by Mativo and Hallinan (2017), to validate the ability of the tool to create compliant mechanisms both symmetric and non-symmetric.

The tool validation for structural designs is affirmed. The tool is however, modified to address the current study.

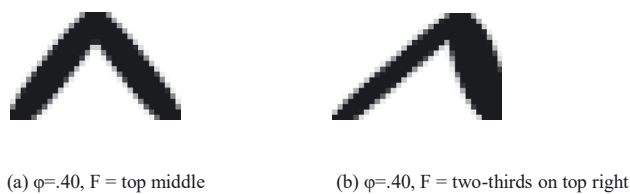


Figure 3.4: Effects of points of load application and support restrictions.

(a) $\varphi = 0.40$, $F = \text{top middle}$ (b) $\varphi = 0.40$, $F = \text{two-thirds on top right}$.

Optimizing for structural model

Table 3.1 lists the design parameters considered for the structural model. These parameters include: design domain, geometry, fixed void region, fixed solid region, variable solid region, fixed nodes, free nodes, uniformly distributed compression loads, shear displacement, adjoint displacement, and mechanical material properties.

The imposed boundary conditions are represented as follows:

- Fixed end: $x_0 = 0$; $x_f = 0$; where x_0 is initial position of x , and x_f is final position of x .
- Free end: $x_L' = 0$; $x_L'' = \delta$; where x_L' is the initial position at the top of the element, and x_L'' is the final position at the top of the element, and δ is the lateral displacement.

Also, the length of the legs is fixed, but the width of the legs can vary subject to the ability to sustain the imposed structural loads.

A matrix determined analytically using symbolic manipulation software by Bendsoe and Sigmund (2004) is modified and used in this numerical experiment. Earlier, in Figure 3.3 an illustration of the elemental degrees of freedom was given. It follows that the matrix terms $k(1)$, $k(2)$, ..., $k(8)$ represent node stiffness. The k_{ij} conditions apply for each node, such that a force in the “i” direction to have a deformation of 1 in the “j” direction only. Table 3.1 provides physical properties of the Young’s modulus and Poisson’s ratio used in the matrix computation. A Young’s modulus (E) of 8.1 and Poisson’s ratio (ν) of 0.23 are used in the matrices.

$$k = \begin{bmatrix} \frac{0.5 - \nu}{6}, \frac{0.125 + \nu}{8}, \frac{0.25 - \nu}{12}, \frac{-0.125 + 3\nu}{8}, \frac{-0.25 + \nu}{12}, \frac{-0.125 - \nu}{8}, \frac{\nu}{6}, \frac{0.125 - 3\nu}{8} \end{bmatrix}$$

$$k_e = \frac{E}{1 - \nu^2} * \begin{bmatrix} k(1)k(2)k(3)k(4)k(5)k(6)k(7)k(8) \\ k(2)k(1)k(8)k(7)k(6)k(5)k(4)k(3) \\ k(3)k(8)k(1)k(6)k(7)k(4)k(5)k(2) \\ k(4)k(7)k(6)k(1)k(8)k(3)k(2)k(5) \\ k(5)k(6)k(7)k(8)k(1)k(2)k(3)k(4) \\ k(6)k(5)k(4)k(3)k(2)k(1)k(8)k(7) \\ k(7)k(4)k(5)k(2)k(3)k(8)k(1)k(6) \\ k(8)k(3)k(2)k(5)k(4)k(7)k(6)k(1) \end{bmatrix}$$

where k_e is the global element stiffness matrix.

Objective function

A representative static load is applied in the design tool to seek a design optimized for the structural loadings. No vibratory loads are applied in the design tool. The process to achieve this desired outcome is to reduce structural material carefully without compromise of structural fidelity. The systematic material reduction is conducted by

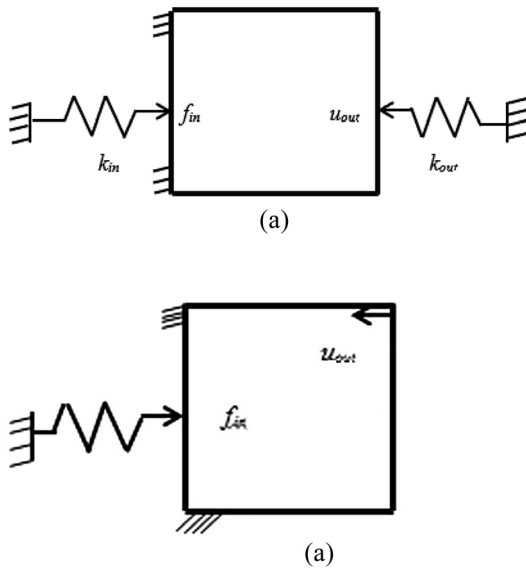


Figure 3.5: (a) A basic compliant symmetric mechanism – example of and load model. (b) Optimized topology of the basic compliant mechanism of (a) (Mativo and Hallinan 2017).

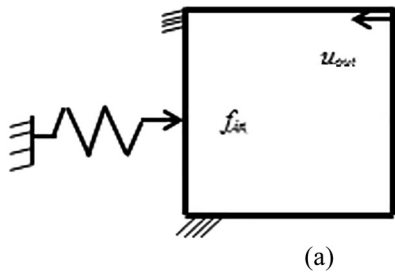


Figure 3.6: (a) A basic compliant non-symmetric mechanism – example of and load model. (b) Optimized topology of the basic compliant mechanism of (a) (Mativo and Hallinan 2017).

Table 3.1: Structural design parameters.

Design parameter	Quantity
Design domain	60 units in x direction 20 units in y direction
Fixed void region	20 in x direction and 16 in y direction
Leg height	16
Leg cross-sectional area space	400
Bismuth telluride density	7.8587 g cm ⁻³
*Bismuth telluride Young's modulus	8.1–50 GPa
Bismuth telluride ultimate tensile strength	7.4 GPa
Bismuth telluride density	7.37 g/cm ³
Bismuth telluride melting point	585 °C
Poisson's ratio	0.23

*Santamaria, Alkorta, and Gil Sevillano (2013) realized a plastic value for Bismuth Telluride under high pressure is assumed to be 3 GPa.

manipulation of the volume fraction for the TEG leg. Therefore, an objective function for maximization of the TEG leg displacement has the form in Eq. (3.3).

$$\max(u) \quad (3.3)$$

subject to the following constraints:

$0 \leq \rho < 1$, i.e., the material distribution (design variable) between 0 and 100%

$$u^* \geq 0.029$$

$$r = 0 = ku - f$$

$$\sum_{e=1}^N v_e \rho_e = V * \varphi, 0 < \rho_{min} \leq \rho_e \leq 1, e = 1, \dots, N$$

where ρ is the element-wise constant material densities in element, $e = 1, \dots, N$. The u^* is the calculated minimum displacement, Eq. (3.4), that is able to supports the loads. The stiffness matrix K depends on ρ . r is the residual in obtaining the structural equilibrium. For topology optimization the equilibrium condition, $r = 0$, is found using an iterative procedure. In this equation, u and f are displacement and load vectors, respectively the shear and adjoint loads are unit valued displacements at the boundary. The displacements can be applied in lieu of a force on a node (Porter 1994).

The preferred displacement u^* should be ≥ 0.029 . This calculated value of 0.029 is considered the minimum displacement from a 100% volume fraction of a unit cell. A displacement greater than u^* would allow the TEG leg to absorb vibrations it currently cannot. The u^* value is obtained using the following equation:

$$u^* = \frac{PL^3}{3EI} \quad (3.4)$$

where P is a point load, L is the length, E is the modulus of elasticity, and I is the inertia.

The goal is to find a maximum displacement of TEG legs that will ensure that the mechanical loads are sustained (i.e., that there is sufficient compliance to tolerate the loads) – ultimately while maintaining the ability to generate maximal power.

Exploring acceptable topologies

The interest in this study is to create compliant TEGs. Therefore, the topology optimization process controls the placement of material in the two legs of the unit cell. A successful optimized structural model requires that

developed TEG should be able to accommodate translation induced by the shear load. Each leg is expected to support translation. A leg with one point connected to the TEGs top cover would allow a minimal lateral displacement before it results to undesired potential rotation. *Two points* connecting the TEG leg to the top cover would allow a higher lateral translation with less induced friction than three or more points would cause. According to Alread and Leaslie (2007), there are three basic ways that structural members can be connected. Pin connection allow members to rotate but not translate, moment connections allow neither translation nor rotation relative to one another, and rollers that allow only translation. Our design follows the latter.

Table 3.2 shows the optimal TEG structures obtained for variable porosity. In the table, the topologies shown in columns 2–4 are created by performing two changes, first by varying the TEG leg width size, an action done by varying width of the street, and secondly by changing the volume fraction or the amount of the TEG material in the legs.

For our case, a baseline model **B** is a topology whose street width size is equal to the width size of each leg as shown in column 3. Topologies with a double street width size **2B**, halves the leg width size, are shown in column 2, while those with half the baseline street width size $\frac{1}{2}B$ are presented in column 4.

The volume fraction is varied from 100 to 60%. This effort is done to examine topologies whether topologies created with a lower volume fraction of TEG material can achieve greater compliance (u) while supporting the structural loads. The volume fraction is presented in column 1, while the displacement is shown in column 5.

Results of the effort presented in Table 3.2 show topologies that are suitable for a vibratory environment and those that are not. A suitable topology is a leg with two points that connect to the top plate. The two points indicate ability for the leg to translate without causing a moment. From the table, and enlarged topologies in Figure 3.7 a and b, it is observed that the baseline models presented in column 3 with a volume fraction around 80% have suitable topologies. Other leg topologies have one point touching the top cover which would restrict desired translation and possibly initiate rotation.



Figure 3.7 a: Suitable leg with two distinct points [1 & 2] touching the top cover.

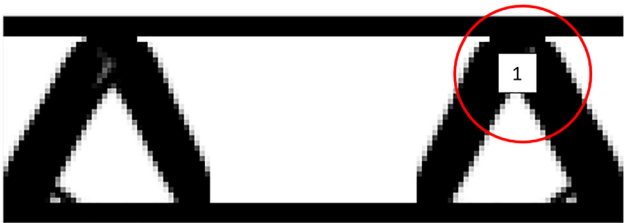













Figure 3.7 b: Unsuitable leg with one point touching the top cover.

Table 3.2: Optimal TEG considering only structural loadings alone for varied leg size.

Volume fraction	$2 \times$ Baseline street ($2B$)	Baseline street (B)	$\frac{1}{2}$ Baseline street ($\frac{1}{2}B$)	Displacement
100				$2B$ ($u = 0.1259$) B ($u = 0.0504$) $\frac{1}{2}B$ ($u = 0.0286$)
90				$2B$ ($u = 0.1259$) B ($u = 0.0555$) $\frac{1}{2}B$ ($u = 0.0376$)
80				$2B$ ($u = 0.1260$) B ($u = 0.0636$) $\frac{1}{2}B$ ($u = 0.0494$)
70				$2B$ ($u = 0.1630$) B ($u = 0.0784$) $\frac{1}{2}B$ ($u = 0.0688$)
60				$2B$ ($u = 0.1902$) B ($u = 0.1031$) $\frac{1}{2}B$ ($u = 0.0962$)

Table 3.3: Percent material, displacements, and topology.

Volume fraction	Displacements (u)	Structural topology
100	0.0504	
90	0.0555	
80	0.0636	
70	0.0784	
60	0.1031	
50	0.1290	
40	0.1420	
30	0.1778	
20	0.2340	
10	0.6079	
0	0.6079	

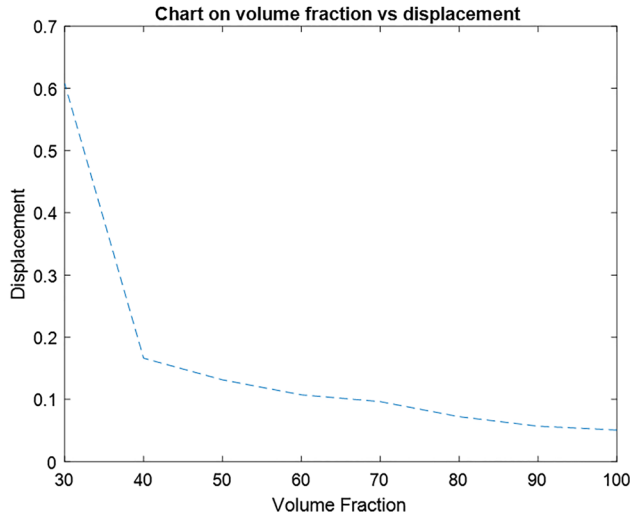


Figure 3.8: Plot of shear displacement versus volume fraction for structurally optimized TEG.

Figure 3.7 a and b are topologies illustrating legs with one, or two points touching the top cover.

Table 3.3 shows the optimal topology as a function of the porosity of the TEG for fixed leg width. Here, the porosity ranges from 0 to 0.8. Each of the shown cases represents the maximum transverse translation at a given porosity. The associated shear translation respectively ranges from 0.0504 to 0.6079. As the porosity increases, the shear translation increases. Thus, more porosity increases the compliance to shear loadings. The largest displacements occurred between volume fractions between 0 and 30%. This displacement is however not considered in this research due to minimal material to even converge and form TEG legs.

Of particular interest is the leg pattern at the top. Topologies with a volume fraction about 80% have two points on each leg. Two points are important because they indicate the ability to accommodate lateral movement at the top of the TEG unit cell which would allow use in a vibratory environment. While Table 3.2 depicts exploration of topologies and displacements of three different leg sizes with variable volume fraction, Table 3.3 presents further exploration of the optimized leg size that emerged from Table 3.2, in pursuit of an optimal displacement as it explores from maximum to minimum volume fractions for the TEG leg.

Figure 3.8 presents the transverse displacement as a function of volume fraction. It is clear that when the volume fraction exceeds 40%, the slope of the displacement reduces markedly. Thus, in a sense, the structural integrity stabilizes rapidly from this point on. In contrast, with a volume fraction

less than 40%, the displacement slope increases rapidly. This may not be bad. If the environment calls for more compliance a higher void percentage is required.

Table 3.4 shows the structurally optimized topologies for volume fractions ranging from 76 to 84%, with the corresponding topologies and displacements shown in columns 2 and 3. It can be observed that the topologies for volume fraction of 80% and above have legs with the same form. The leg topology at a volume fraction of 78% displays a slightly different form for each leg, which could be a concern for even translation. The optimal topology associated with a 76% volume fraction has legs connected only at one point at the top cove. Therefore, the topologies associated with volume fractions beneath 80% here are not feasible.

Optimizing for only thermal

Thermal model

Optimal topologies for thermal loadings alone based upon the logic shown in the flowchart given by Figure 3.2 are likewise developed for variable volume fractions. A one-dimensional steady-state heat conduction model is assumed for the unit cell.

The heat transfer rate is governed by Fourier's Law (Eq. (3.5))

$$q_x = -kA \frac{\partial T}{\partial x} \quad (3.5)$$

where q_x is the x -component of the heat transfer rate, k is thermal conductivity of the material, A is the area normal to heat flow, and $\frac{\partial T}{\partial x}$ is the temperature gradient. When the length, l , of the member or element is considered, Eq. (3.9) can be re-written as (Eq. (3.6))

$$q = \frac{kAdT}{l} \quad (3.6)$$

Since we have a constant thermal conductivity, k , Laplace's equation governs the change in temperature in the x -direction.






$$\frac{d^2 T}{dx^2} = 0 \quad (3.7)$$

Integrating Eq. (3.7) twice results in Eq. (3.8).

$$T(x) = c_1 x + c_2 \quad (3.8)$$

To solve for c_1 and c_2 , we assume two boundary equations as follows: at $x = x_0$, $T = T_0$, and at $x = x_L$, $T = T_L$.

Table 3.4: Structurally optimized topologies for volume fraction near 80%.

Volume fraction (%)	Topologies	Displacement (μ)
84		0.0604
82		0.0620
80		0.0636
78		0.0662
76		0.0688

The solution to Eqs. (3.7) and (3.8) are as follows in Eqs. (3.9a) and (3.9b).

$$c_1 = \frac{T_0 - T_L}{x_L - x_0} \quad (3.9a)$$

$$c_2 = T_0 + \left[\frac{T_0 - T_L}{x_L - x_0} \right] x_L \quad (3.9b)$$

Similar to the structural model, the thermal model has a conductance matrix $[K]$, a temperature matrix $\{T\}$, and the heat source matrix $\{q\}$. These matrices are created and assembled for each leg and computed to find thermal flow depicted as $q = KT$. Following the procedure of Bendsoe and Sigmund (2004), a 4×4 conductance matrix was developed to describe the thermal model.

$$k_e = \begin{bmatrix} \frac{2}{3}, \frac{-1}{6}, \frac{-1}{3}, \frac{-1}{6} \\ \frac{-1}{6}, \frac{2}{3}, \frac{-1}{6}, \frac{-1}{3} \\ \frac{-1}{3}, \frac{-1}{6}, \frac{2}{3}, \frac{-1}{6} \\ \frac{-1}{6}, \frac{-1}{3}, \frac{-1}{6}, \frac{2}{3} \end{bmatrix}$$

Here k_e is thermal conductance.

The heat conductance in a global form can be written as $K_{th}T = F_{th}$. T is the temperature, and F_{th} is the thermal load vector which characterizes the heat flux at the boundary. K_{th} is the conductivity matrix and takes the form

$$K_{th} = \sum_{e=1}^N K_{th}^e \rho \quad (3.10)$$

where N is the number of elements, and ρ is the design variable. The elemental thermal conductivity K_{th}^e is given by:

$$\frac{Q}{t} = kA \frac{\Delta T}{d} \quad (3.11)$$

Here, Q/t is the rate of thermal energy transferred through the material. The thermal conductivity is represented by k . The cross-sectional area is represented by A . The difference in temperature is represented by ΔT . The thickness or length through which heat transfers is represented by d .

The thermal design parameters shown in Table 3.5 include geometrical characteristics, material properties, and heat source and heat sink temperatures.

Ultimately, the maximum heat flow is dependent on the structure. Rowe (2006), states that the ideal geometry for thermo-elements used in TEGs should be long and thin (p. 1–11).

Objective function

In this model, the TEG legs are assumed to be made of homogenous material (Figure 3.9). The leg volume has a uniform cross-sectional area and perfect insulation is assumed for all sides.

The desired objective is to maximize the temperature gradient by maximizing heat flow through the TEG. The objective function for the quest is shown in Eq. (3.12).

$$\max(q) \quad (3.12)$$

subject to the following constraints:

$0 \leq \rho < 1$, i.e., the material distribution (design variable) between 0 and 100%

$$T_{\min} \leq T \leq T_{\max}$$

$$\sum_{e=1}^N v_e \rho_e = V^* \varphi, 0 < \rho_{\min} \leq \rho_e \leq 1, e = 1, \dots, N$$

where ρ are the element-wise constant material densities in element, $e = 1, \dots, N$.

Maximizing the heat flow through the TEG legs by varying volume fraction φ , subject to the equilibrium constant $[K_{th}T - F_{th} = 0]$ and material volume constraint $\sum_{e=1}^N v_e \rho_e \leq V, 0 < \rho_{\min} \leq \rho_e \leq 1$, when $e = 1, \dots, N$ are used in the analysis; and its conductivity captured in Eq. (3.10).

Cases examined

Optimal topologies were developed for varying volume fraction, as shown in Figure 3.10 below. Figure 3.7 a–c show the optimal topologies for respectively 100, 80, and 60% volume fractions.

The heat conductance patterns mirror Bejan's Constructal Law (Bejan 2005, 2015; Bejan and Lorente 2008a; Bejan, Lorente, and Lee 2008b). These researchers argued

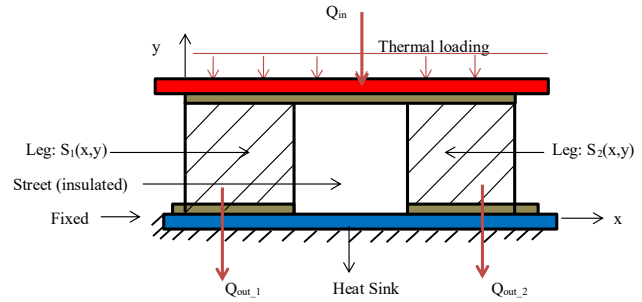


Figure 3.9: TEG unit cell subject to thermal loading.

that for a flow system to persist in time it must evolve in such a way that it provides easier access to its currents, as supported by Bejan's Constructal Law of tree like flow patterns. Further, in his observation, Bejan suggested that nature is the law of configuration generation, or the law of design. Where others saw disorder, Bejan found a pattern. "One of the basic aims of design is to get the most amount of work done with the least amount of effort. What engineers try to accomplish through their plans, nature achieves on its own. Zane (2007) wrote about going with the flow and gave examples such as animate (people, trees) and inanimate (rivers, mud cracks) phenomenon, if given freedom, will organize themselves into patterns or shapes that help them get from here to there in an easier manner".

Multi-functional optimization for combined structural and thermal loads

In this section, a general multi-dimensional optimization approach is considered, whereby an optimal topology can be developed to maximize for displacement and heat flux. The weighting of structural and thermal densities is represented by Eq. (3.13).

$$c = w_s u + (1 - w_s) q. \quad (3.13)$$

Above, c is the objective function, w_s is the weight by eight structural matrix, u is the displacement, and q is the heat flux. Effectively, these weightings define which model is more important.

Equations (3.13) can also be expressed as:

$$\max(u, q) = k_1 u + k_2 q \quad (3.14)$$

where k_1 is the structural matrix, and k_2 is the thermal matrix. Both Eqs. (3.13) and (3.14) are used to find the optimal densities (e.g., localized void fraction) for the given weightings of the thermal and structural models.

Table 3.5: Thermal design parameters.

Design parameter	Quantity
Design domain	60 units in x direction 20 units in y direction
Fixed void region	20 in x direction and 16 in y direction
Leg height	16
Leg cross-sectional area space	400
Bismuth telluride seebeck coefficient, α_p, α_n	0.000215, -0.000215 v K ⁻¹
Bismuth telluride thermal conductivity, k_p, k_n	1.47 Wm ⁻¹ K ⁻¹
Temperature – heat source	110 °C < T ≤ 230 °C
Temperature – heat sink	50 °C

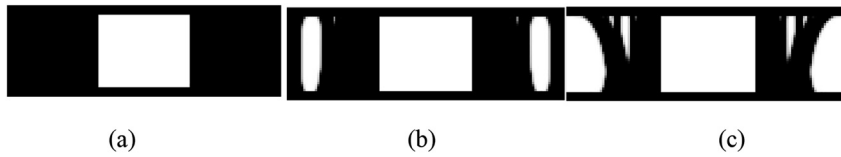


Figure 3.10: Optimal topologies for volume fractions of (a) 100%, (b) 80%, and (c) 60%.

Results are shown in Table 3.6 for a volume fraction of 0.8 only. No other results were obtained as this approach is generally not useful. The reality is that the goal always will be to generate the most power (maximize heat flux) while ensuring that the structural loads are accommodated. Thus, mechanical loads represent a constraint; not something to be optimized.

As shown in the table, a weighting of about w_s of 0.4 yielded the best combination for heat flux and displacement.

Shape optimal solutions were developed for TEG legs for variable volume fraction of material. With boundary conditions in place, models were created to study thermal flow effects and patterns. This exercise was intentional because we wanted to investigate thermal flow for an optimal structural model. A heat source of a constant temperature 230 °C was applied and a heat sink temperature of 50 °C was set.

Table 3.7 shows different patterns for structural only and thermal only loadings. Shown are shape optimal solutions for material volume fractions of 100, 80, and 60% for separate thermal and structural loadings. In all thermal models, a uniform heat load is distributed across the upper face of the top plate. At the bottom face, the material is contiguous. The topologies created match those obtained in the previous sections for respectively structural and thermal optimization alone.

Table 3.6: Search for best combination of heat flux and displacement.

Weighting solid (w_s)	Heat flux (q)	Displacement (u)
0	0.302	0
0.1	0.272	0.045
0.2	0.242	0.091
0.3	0.211	0.136
0.4	0.181	0.182
0.5	0.151	0.227
0.6	0.121	0.272
0.7	0.091	0.312
0.8	0.061	0.364
0.9	0.031	0.410

Optimization of TEG power for combined structural and thermal loads

Power generation in a TEG is a function of the leg geometry, figure of merit (ZT), thermal conductivity, and electrical resistivity. In traditional thermoelectric designs, TEG legs have constant cross-sectional which lend them to be applied into thermoelectric equations easily. Because we are optimizing for power (thermal loads), a constant cross-sectional area is assumed to simplify analysis. In reality, because the heat flow through a TEG with distance from the source declines slightly, one could relax this assumption. However, maximal TEG power conversion efficiencies based upon the second Law of Thermodynamics are no greater than 0.1, the assumption for constant cross-section is reasonable.

TEG heat conversion to power

Three phenomena control the power generation within a TEG; namely the Seebeck effect, Joule effect, and Thomson effect.

The Seebeck effect describes how a temperature difference between two dissimilar conductors produces electromotive force between them. The p -type leg contains positive charge carrier (holes) while the n -type leg is a negative charge carrier (electrons). If the hot and cold junctions are maintained at different temperatures T_h and T_c and $T_h > T_c$, an open circuit electromotive force, V , is developed at the resistance load, R_L . This action is represented in Eq. (3.15):

$$V = \alpha(T_h - T_c) \text{ or } \alpha = V/\Delta T \quad (3.15)$$







where V is electromotive force or voltage, α is Seebeck coefficient, T_h is temperature at the heat source, and T_c is temperature at the sink.

The electromotive force is a catalyst for the thermally excited electrons to move. Although the temperature distribution along the legs is the same, the heat flux is higher in the n -type leg. Different charge carriers in the legs cause unique rate of vibrations resulting to current flow.

Joule heating occurs when current flows through a material offering resistance to the flow. The amount of heat produced is represented as shown in Eq. (3.16).

$$Q_j = I^2 R \quad (3.16)$$

Table 3.7: Topology differences of structural only and thermal only loadings.

Percentage volume fraction	Structural only topology under compression and shear loads	Thermal only topology
100		
80		
60		

where Q_j is joule heating, I is current, and R is electrical resistance.

The Thomson effect relates to the rate of generation of reversible heat resulting from the flow of current along an individual conductor along which there is a temperature difference (Rowe 2006; Ruiz-Ortega and Olivares-Robles 2018; Saqr and Musa 2009). The Thomson effect is defined by Eq. (3.17).

$$Q_t = \beta I \Delta T \quad (3.17)$$

where β is the Thomson coefficient, Q_t is the rate of reversible heat absorption, I is the current flow, and ΔT is the temperature difference between the ends of the conductor. This effect is normally minimal.

The performance of the thermoelectric generator is greatly influenced by the figure of merit (Z) depicted in Eq. (3.18) below.

$$Z = \frac{\alpha^2 \sigma}{k} \quad (3.18)$$

Here $\alpha^2 \sigma$ is the electrical power factor and k is the thermal conductivity. When multiplied with temperature, Z becomes unitless and is represented as ZT , a dimensionless figure of merit. A higher ZT is associated with higher TEG power generation. Further, in order to obtain maximum figure of merit (Kanimba and Tian 2016), the geometry and material properties for the TEG should satisfy Eq. (3.19) (Chen, Meng, and Sun 2012; Kanimba and Tian 2016; Rowe 2006).

$$\frac{A_p^2 L_n^2}{A_n^2 L_p^2} = \frac{k_n \rho_p}{k_p \rho_n} \quad (3.19)$$

where A_p is cross sectional area positive leg, A_n is cross

sectional area negative leg, L_n is length negative leg, L_p is length positive leg, k_n is thermal conductivity negative leg, k_p is thermal conductivity positive leg, ρ_p is electrical resistivity positive leg, and ρ_n is electrical resistivity negative leg.

The continuity equation for the steady-state current flow in a thermoelectric material can be represented as

$$\vec{\nabla} \cdot \vec{j} = 0. \quad (3.20)$$

where $\vec{\nabla}$ is the differential operator with respect to length and \vec{j} is the current density. The current density \vec{j} and temperature gradient $\vec{\nabla} T$ affect the electric field \vec{E} . Differentiating Eq. (3.18) with respect to length results to an electric field shown in Eq. (3.21) (Lee 2013).

$$\vec{E} = \vec{j} \rho + \alpha \vec{\nabla} T \quad (3.21)$$

where ρ is electrical resistivity and α is Seebeck coefficient.

The heat flux is represented as (Eq. (3.22))

$$\vec{q} = \alpha T \vec{j} - k \vec{\nabla} T \quad (3.22)$$

The heat diffusion for a steady state is given as (Eq. (3.23))

$$-\vec{\nabla} \cdot \vec{q} + \dot{q} = 0 \quad (3.23)$$

where \dot{q} is expressed as shown in Eq. (3.24)

$$\dot{q} = \vec{E} \cdot \vec{j} = J^2 \rho + \vec{j} \cdot \alpha \vec{\nabla} T \quad (3.24)$$

Substituting Eqs. (3.22) and (3.24) into Eq. (3.23), results in Eq. (3.25)

$$\vec{\nabla} \cdot (k \vec{\nabla} T) + J^2 \rho - T \frac{d\alpha}{dT} \vec{j} \cdot \vec{\nabla} T = 0 \quad (3.25)$$

where $\vec{\nabla} \cdot (k \vec{\nabla} T)$ is thermal conduction, $J^2 \rho$ is Joule heating, and $T \frac{d\alpha}{dT}$ is the Thomson coefficient (Lee 2013).

Examining one dimension heat transfer

The governing equations given by Eqs.(3.20)–(3.25) simplify significantly with a one-D heat flow assumption, which is appropriate given the assumption of constant cross-sectional area and nearly constant heat flow in the y -direction. Thus, the energy balance given by Figure 3.11 can represent the heat and power flow through a thermoelectric leg with $x = L$ being the hot side and $x = 0$ depicting the cold side. The schematic below represents the global energy balance on a leg.

A differential energy balance inclusive of the Thomson and Joule heating terms is thus given by Eq. (3.26) (Lee 2013):

$$-Q|_{k,x} + Q|_{k,x+\Delta x} + Q_\mu + Q_j = 0 \quad (3.26)$$

Further, using Fourier's Law and the definitions for Joule and Thomson heating given respectively by Eqs. (3.16) and (3.17), Eq. (3.26) can be expressed as

$$\frac{d}{dx} (T + \Delta T)kA - \frac{dT}{dx}kA + \mu eJA\Delta T + (eJ)^2 \frac{AL}{\sigma} \frac{\Delta x}{L} = 0 \quad (3.27)$$

and re-written as

$$kA \frac{dT}{dx} \Big|_{x+\Delta x} - kA \frac{dT}{dx} \Big|_x + \mu eJA\Delta T + (eJ)^2 \frac{AL}{\sigma} \frac{\Delta x}{L} = 0 \quad (3.28)$$

where T , k , A , μ , eJ , σ , and L are respectively temperature, thermal conductivity, cross section area, Thomson coefficient, electrical current density, electrical conductivity, and length of a TEG leg.

The boundary conditions given by Eqs. (3.29) and (3.30) are applied to Eq. (3.28),

$$T_p(x=0) = T_n(x=0) = T_c \quad (3.29)$$

$$T_p(x=L_p) = T_n(x=L_n) = T_h \quad (3.30)$$

Here the subscripts c, and h represent cold side (heat sink), and hot side (heat source), respectively; and then taking the limit as Δx goes to 0, the following differential Eqs. (3.31) and (3.32) result for the p - and n -type legs.

p -type leg

$$k_p A_p \frac{d^2 T_p}{dx^2} + \mu_p I \frac{dT_p}{dx} + \frac{I^2}{\sigma_p A_p} \quad (3.31)$$

n -type leg

$$k_n A_n \frac{d^2 T_n}{dx^2} - \mu_n I \frac{dT_n}{dx} + \frac{I^2}{\sigma_n A_n} \quad (3.32)$$

where $I = eJA$ is the electrical current.

The heat flow through each of the legs is given respectively by Eqs. (3.31) and (3.32) for respectively the hot and cold sides of the TE.

$$Q_h = N \left(\alpha I T_h + k_p A_p \frac{dT_p}{dx} \Big|_{x=L_p} + k_n A_n \frac{dT_n}{dx} \Big|_{x=L_n} \right) \quad (3.33)$$

$$Q_c = N \left(\alpha I T_c + k_p A_p \frac{dT_p}{dx} \Big|_{x=0} + k_n A_n \frac{dT_n}{dx} \Big|_{x=0} \right) \quad (3.34)$$

where α is the Seebeck coefficient and represents $\alpha_{ph} - \alpha_{nh}$ for $x = L$, and $\alpha_{pc} - \alpha_{nc}$ for $x = 0$. These equations can be further simplified by using the following relationship for thermal and electrical conductance given by Eqs. (3.35) and (3.36).

$$K = \frac{k_p A_p}{L_p} + \frac{k_n A_n}{L_n} \quad (3.35)$$

$$R = \frac{L_p}{\sigma_p A_p} + \frac{L_n}{\sigma_n A_n} \quad (3.36)$$

Using Eqs. (3.29), (3.30) and (3.33)–(3.36), we can generate Eqs. (3.37) and (3.38)

$$Q_h = N \left(\alpha_h I T_h + K \Delta T - \frac{1}{2} I^2 R - \frac{1}{2} \mu I \Delta T \right) \quad (3.37)$$

$$Q_c = N \left(\alpha_c I T_c + K \Delta T + \frac{1}{2} I^2 R + \frac{1}{2} \mu I \Delta T \right) \quad (3.38)$$

The equation to determine power is given as

$$P = Q_h - Q_c = N(\alpha I \Delta T - I^2 R) \quad (3.39)$$

The equation used to calculate the thermal power efficiency of the TEG is

$$\eta = \frac{P}{Q_h} \quad (3.40)$$

Power output in a thermoelectric generator is a function of electrical current. In this case, the interest is in flexibility of the TEG leg, and the power that could be generated in that state. In addition, although shown in Eqs. (3.37) and (3.40), the Thomson effect is neglected in this thermoelectric computation as it has been identified as having minimal influence (Rowe 2006).

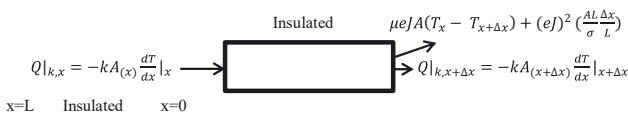


Figure 3.11: Illustration of equations used to evaluate heat conduction through a TEG leg.

The integrated model is a function of separately running the structural model matrices and thermal/power model matrices with their results normalized, weighted and combined to obtain optimized outcomes (Mativo and Hallinan 2017). The reason to run the two models separately is because of their uneven degrees of freedom (dof) that originate from differences in their discrete elements in the reference domain. The structural element node has the potential to translate (x, y, z) and the ability to rotate (x, y, z). This operation results to six dofs. The thermal element node can only translate (x, y, z) and hence has three dofs. All the boundary conditions stated for both structural and thermal models apply in the integrated model.

Integrated model

The combined model is used to examine what heat flow can be allowed subject to the constraint of meeting applied loads. Design parameters for both structure and thermal are presented in Table 3.8.

The objective function for the combined structural and thermal load is shown as maximizing displacement and maximizing heat flow as represented by:

$$\max(u, q) \quad (3.41)$$

subject to the following constraints:

Table 3.8: Design parameters for integrated model.

Design parameter	Quantity
Design domain	60 units in x direction 20 units in y direction
Fixed void region	20 in x direction and 16 in y direction
Leg height	16
Leg cross-sectional area space	400
Bismuth telluride density	7.8587 g cm^{-3}
Bismuth telluride Young's modulus	$8.1\text{--}50 \text{ GPa}$
Bismuth telluride ultimate tensile strength	7.4 GPa
Bismuth telluride density	7.37 g/cm^3
Bismuth telluride melting point	$585 \text{ }^\circ\text{C}$
Bismuth telluride seebeck coefficient, α_p, α_n	$0.000215, -0.000215 \text{ v K}^{-1}$
Bismuth telluride thermal conductivity, k_p, k_n	$1.47 \text{ Wm}^{-1} \text{ K}^{-1}$
Temperature – heat source	$110 \text{ }^\circ\text{C} < T \leq 230 \text{ }^\circ\text{C}$
Temperature – heat sink	$50 \text{ }^\circ\text{C}$
Poisson's ratio	0.23

$0 \leq \rho < 1$, i.e., the material distribution (design variable) between 0 and 100%

$$T_{\min} \leq T \leq T_{\max}$$

$$\mathbf{u}^* \geq 0.029$$

$$\mathbf{r} = \mathbf{0} = \mathbf{K}\mathbf{u} - \mathbf{f}$$

$$\sum_{e=1}^N v_e \rho_e = V^* \varphi, 0 < \rho_{\min} \leq \rho_e \leq 1, e = 1, \dots, N$$

where ρ is the element-wise constant material densities in element, $e = 1, \dots, N$. T_{\min} is the temperature at the heat sink, while T_{\max} is the temperature at the heat source. The \mathbf{u}^* is the minimum calculated displacement. The stiffness matrix \mathbf{K} depends on the ρ . \mathbf{r} is the residual in obtaining the structural equilibrium. For topology optimization the equilibrium $\mathbf{r} = \mathbf{0}$ is found using an iterative procedure. \mathbf{u} and \mathbf{f} are displacement and load vectors, respectively.

The MATLAB tool used for the structural model and thermal models were significantly modified to integrate both models and calculate power. The flow chart illustrated in Figure 3.12 depicts the process. It shows a tool that simultaneously computes a TEG leg topology by distributing available material in the integrated design domain and creating corresponding heat path resulting to a reconfigured leg and power generation, respectively.

The MATLAB code for the combined model is divided into five sections. The first main section of the program defines the inputs and starts the distribution of the material evenly in the design domain. An initialization of design variables and physical variables is done. In this case, the design variable is the volume fraction limit of the material that is used to develop optimal topologies for special TE material volume fractions. The physical densities are initially assigned a constant uniform value, but are iteratively updated to form an optimal ability to support both structural and thermal loads. A power-law approach is used to penalize intermediate density values, driving them towards solid or void.

The second code section is the Optimality Criteria (OC) which updates the design variables depending on the used and remaining material. The OC is formulated on the conditions that if constraint $0 \leq x \leq 1$ is active, then convergence is achieved with a positive move-limit of 0.2 and a damping factor of 0.3, for compliant designs (Bendsoe 1995; Liu and Tovar 2014; Vijayan and Thangavelu 2012). Material spread entirely on an element is considered to have a value of 1, while an element without any material has a value of 0. The

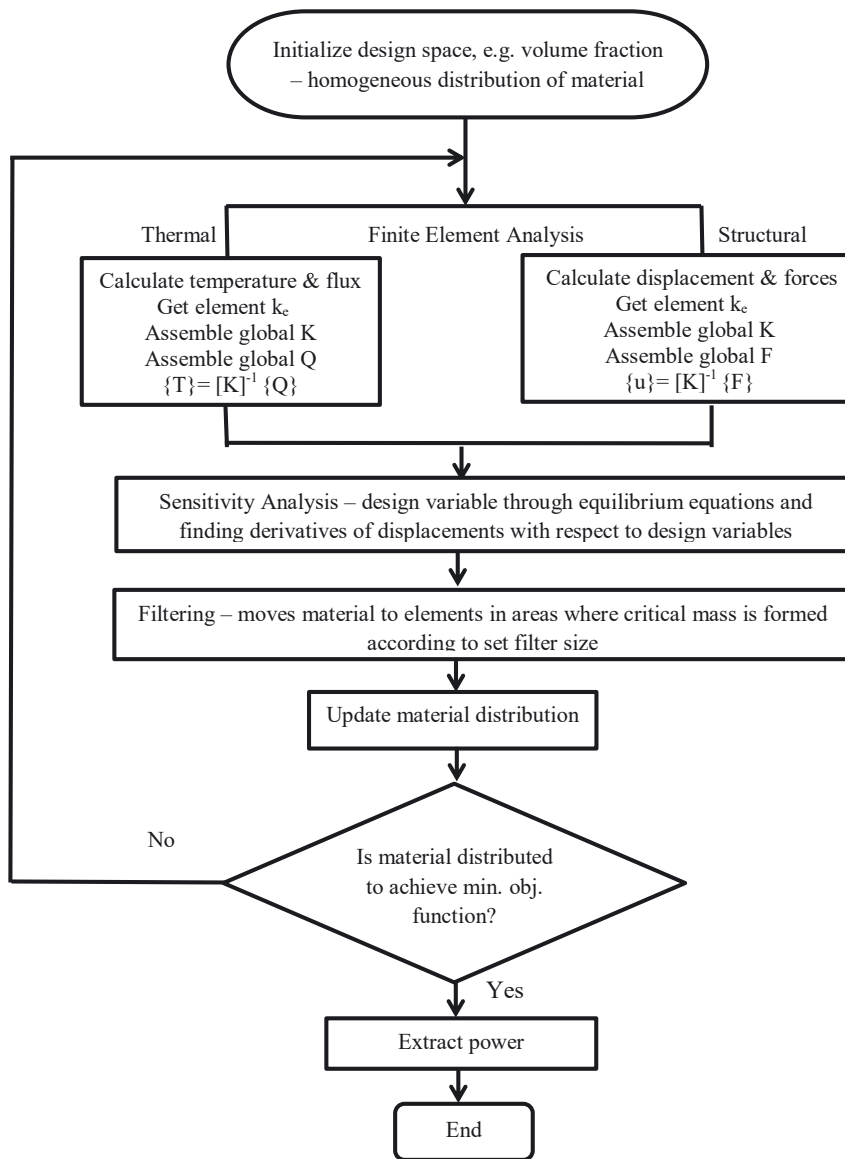


Figure 3.12: Detailed flowchart of integrated TEG model with power extraction.

iterative process continues with termination occurring when a maximum number of iterations is reached or where a tolerance of the material distribution is relatively small, for example if available material is equal to or less than 0.01 (Liu and Tovar 2014).

In the third section of the code, a mesh-independency filter whose function is to avoid numerical instabilities is applied. The filtered density defines a modified physical density that is now incorporated in the topology optimization formulation. During each iteration, the element sensitivity is modified. This process ensures that elements gain or lose material depending on the critical amount available and reaction loads, based on set filter settings.

The finite element code is the fourth section of the program. Here, two separate global stiffness matrices are simultaneously created by a loop over all elements and executed. A four node bi-linear element enables formation of an 8×8 stiffness matrix for structural loading while a 4×4 heat conduction matrix is formed for the mono-linear thermal element. The two matrices evaluation simultaneously is the uniqueness of the tool. Both matrices are weighted and normalized for optimized topologies before power extraction.

Finally, the fifth section of the code addresses calculation of the power generation. It should be noted that while the goal is to maximize power generation; the reality is that maximizing heat flux is the equivalent of this.

Results

Numerical experiments were conducted to study the integrated structural and thermal with power generation. Shear loading cases that were used in the structural only models are also applied to the integrated models and the resulting adjoint displacements calculated. The integrated models use optimized structural models and seek to maximize heat flux. In order to achieve an even structural and thermal density in the design domain, the baseline model at 100% volume fraction was used to determine the objective functions for both the structural and thermal models. For the structural model, both the mechanical loads and the constraints were applied resulting to an objective function of 57.43. For the thermal model, both the thermal loads for the heat source and heat sink; and constraints of insulated sides were applied resulting to an objective function of 79.91. Together their total was 137.34 which made the structural density to be at 41.8% and thermal to be 58.2%. To normalize the density to a 50–50 ratio, the density for the structure was multiplied by 1.2 while the thermal was multiplied by 0.86.

Table 3.9 shows the effects of optimization weighting on topologies. Weighting is done between 0 (thermal only) and 1 (structural only). It was observed that the higher the structural weighting, the less the displacement and the increase in power generated.

Table 3.10 shows the optimal configurations for representative results for volume fractions ranging from 100 to 40%. Volume fractions between 30 and 0% have no material to create a leg to allow heat transport. As seen, unique topologies form when structural and thermal loads are simultaneously applied to varying volume fractions. Consistently,

most of the heat transport occurs along the street where the most material is found. From the topologies, it is observed that the overall constraint is structural because in the end it provides a path to heat flow. The heat travels to the sink where it is readily distributed. A lower volume fraction yields more displacement at the cost of less power generated. In order to sustain shear load, less material is required, which means that the thermal resistance increases. Thus, for a given temperature difference, there is reduced heat transfer, and thus power generation potential.

Power generation is favored highly with models that have more material. The highest power generation is shown to be from the model without a void while the least power generation has the least material. Power generated from models with volume fraction of 50% and less are not to be considered because they are not structurally capable of supporting all loads. Comparisons of maximum power generation for the baseline model, and the reconfigured integrated model are shown in Table 3.11.

The aim of this study was to search for TEG geometry that could be used in a vibratory environment. Based on the investigation, several models emerged with different potentials. Tradeoffs are seen in Table 3.11 and in Figure 3.13. Figure 3.13 presents a relationship between displacement and power generation. As can be seen, the less the displacement, the higher the power generation. This is expected because there is more material to carry heat.

The less void in the leg, the higher the power and less shear displacement. For a balanced model that power generates and is structurally stable, a 80% volume fraction is recommended for it can allow a displacement of 0.0636 and produce about 80% baseline power.

Table 3.9: Effects of weighting (Ws) on the combined model.











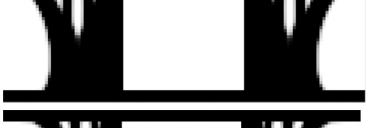


Percent structural weighting (Ws)		Percent structural weighting (Ws)	
0		0.2	
0.4		0.6	
0.8		1	

Table 3.10: Displacement, power, and shape of an integrated TEG for the vibratory environment.

Volume fraction	Displacement	Power generation at 110 °C	Power generation at 170 °C	Power generation at 230 °C	Shape
100	0.0504	0.1163	0.4467	1.0499	
90	0.0555	0.1078	0.4319	0.9725	
80	0.0636	0.0992	0.3972	0.8937	
70	0.07841	0.0900	0.3604	0.8115	
60	0.1031	0.0799	0.3231	0.7264	
50	0.1290	0.0704	0.2824	0.6374	
40	0.1420	0.0591	0.2362	0.5313	

Conclusion

This study successfully investigated the development of flexible TEGs that can potentially be used in vibratory environment thus increasing the reach of locations that can be accessed for energy harvesting. First, a numerical tool was created to perform TEG unit cell numerical experiments. The creation of the tool required a creation of a design domain where material distribution would be done to study effects of creating a TEG unit cell with varying volume fraction. Structural boundary conditions of fixed and free nodes, fixed solid region, and fixed void region, compression load, shear displacement, and adjoint displacement were applied to the design domain. A Marlow TG 12-6 was used as baseline for this study. A baseline TEG unit cell model was successfully created and tested. Once baseline parameters were established, numerical experiments for structural only model were conducted with the

aid of varying material distributed within the design domain to establish compliant designs. Various structural topologies were created and studied. The optimal structural only compliant topology was established.

Next, thermal boundary conditions were added to the structural model and tested for heat flow patterns. It was shown that some of the compliant models had void areas that prevented heat flow across the legs. The study helped in determining the model used in the integrated model. The integrated model was a combination of structural and thermal loading, and power extraction. A successful integrated model was established and presented in the paper. With a range of new integrated TEG legs that offer opportunity for energy harvesting in vibratory environments, it is expected that more waste heat, previously not accessible due to vibratory environments, can be reached and converted to electricity.

Limitations to this study include the assumptions of constant heat flux, constant cross-sectional area, and the

Table 3.11: Maximum power generation for the baseline and the integrated model.

Experiment/temperature	Baseline	Integrated
230 °C	1.0499	0.8937
170 °C	0.4667	0.3972
110 °C	0.1163	0.0992

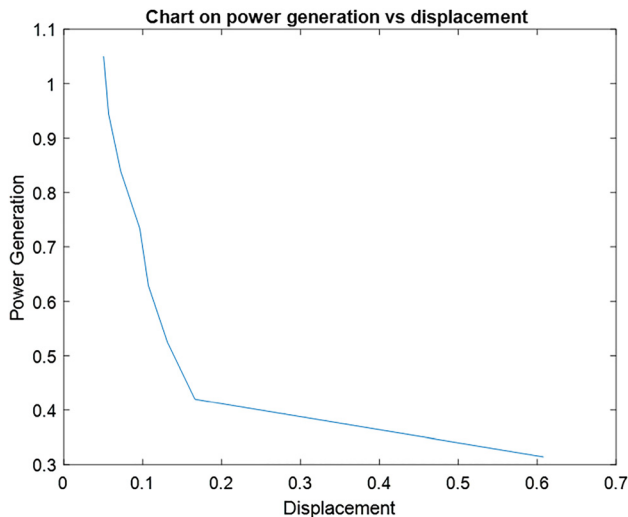


Figure 3.13: Chart display power generation versus displacement.

assumption of 1-D heat transfer. The assumptions allowed us to use the continuity equation for steady-state current flow. In addition, the assumption of a constant-cross-sectional area, and nearly heat flow in one direction, allowed us to use the 1-D heat flow equations. These assumptions significantly simplified the equations used. We believe in the results and trust they are helpful to build upon.

In order to access more waste heat sites for energy harvesting, more research is necessary for the development of flexible TEGs. Our contribution indicates that by reconfiguring the design or shape of a TEG leg, shear displacement can be allowed. Physical experiment to verify our numerical experiment will be very helpful to learn how well it works in a physical environment. Also, a similar study as ours with filler material in the void TEG leg spaces will inform improved strength and improved power generation.

Author contributions: All the authors have accepted responsibility for the entire content of this submitted manuscript and approved submission.

Research funding: None declared.

Conflict of interest statement: The authors declare no conflicts of interest regarding this article.

References

- Agabaev, C., G. K. Kotylo, S. Khandovletov, V. G. Sholopov, and A. S. Styagov. 1979. "Metallic Thermoelectric Materials in Solar Thermoelectric Generators." *Applied Solar Energy* 15: 6.
- Alread, J., and T. Leslie. 2007. *Design-Tech: Building Science for Architects*. Oxford: Architectural Press – Elsevier.
- Ambrosi, R. M., H. Williams, E. J. Watkinson, A. Barco, R. Mesalam, T. Crawford, C. Bicknell, P. Samara-Ratna, D. Vernon, N. Bannister, D. Ross, J. Sykes, M. C. Perkinson, C. Burgess, C. Stroud, S. Gibson, A. Godfrey, R. G. Slater, M. J. Reece, K. Chen, K. Simpson, R. Tuley, M. Sarsfield, T. P. Tinsley, K. Stephenson, D. Freis, J. F. Vigier, R. J. M. Konings, C. Fongarland, M. Libessart, J. Merrifield, D. P. Kramer, J. Byrne, and B. Foxcroft. 2019. "European Radioisotope Thermoelectric Generators (RTGs) and Radioisotope Heater Units (RHUs) for Space Science and Exploration." *Space Science Review* 215: 55.
- Arora, S., V. Jaimini, S. Srivastava, and Y. K. Vijay. 2017. "Properties of Nanostructure Bismuth Telluride Thin Films Using Thermal Evaporation." *Journal of Nanotechnology* 2017: 4276506 (4 pages).
- Bejan, A. 2005. "The Constructal Law of Organization in Nature: Tree-Shaped Flows and Body Size." *Journal of Experimental Biology* 208: 1677–86.
- Bejan, A. 2015. "Constructal Law: Optimization as Design Evolution." *Journal of Heat Transfer-transactions of The ASME* 137 (6): 061003 (8 pages).
- Bejan, A., and S. Lorente. 2008a. *Design with Constructal Theory*. New York: John Wiley & Sons. Also available at http://media.wiley.com/product_data/excerpt/68/04719981/0471998168.pdf.
- Bejan, A., S. Lorente, and J. Lee. 2008b. "Unifying Constructal Theory of Tree Roots, Canopies, and Forests." *Journal of Theoretical Biology* 254 (3): 529–40.
- Bell, L. E. 2008. "Cooling, Heating, Generating Power, and Recovering Waste Heat with Thermoelectric Systems." *Science* 321: 1457–61.
- Bendsoe, M. P. 1995. *Optimization of Structural Topology Shape and Material*. New York: Springer-Verlag Berlin Heidelberg.
- Bendsoe, M. P., and O. Sigmund. 2004. *Topology Optimization: Theory, Methods and Applications*, 2nd ed. Corrected printing. Berlin: Springer-Verlag.
- Chen, L., F. Meng, and F. Sun. 2012. "Maximum Power and Efficiency of an Irreversible Thermoelectric Generator with a Generalizable Heat Transfer Law." *Scientia Iranica* 19 (5): 1337–45.
- Choi, H. S., W. S. Seo, and D. K. Choi. 2011. "Prediction of Reliability on Thermoelectric Module through Accelerated Life Test and Physics-of-Failure." *Electronic Materials Letters* 7 (3): 271–5.
- Crane, D. T., and L. E. Bell. 2006. "Progress Towards Maximizing the Performance of a Thermoelectric Power Generator." In *ICT Proceedings ICT06 – 25th International Conference on Thermoelectrics*, 11–6. IEEE. <https://doi.org/10.1109/ICT.2006.331259>.
- DiSalvo, F. J. 1999. "Thermoelectric Cooling and Power Generation." *Science* 285: 703–6.
- Glatz, W., S. Muntwyler, and C. Hierold. 2006. "Optimization and Fabrication of Thick Flexible Polymer Based Micro Thermoelectric Generator." *Sensors and Actuators A* 132 (2006): 337–45.
- Goldsmid, H. J. 2016. *Introduction to Thermoelectricity*. Germany: Springer-Verlag GmbH Berlin Heidelberg.

- Hashim, H., J. J. Bomphery, and G. Min. 2016. "Model for Geometry Optimization of Thermoelectric Devices in a Hybrid PV/TE System." *Elsevier. Renewable Energy* 87: 458–63.
- James, A. B. 1962. "Solutions to Differential Equations Describing the Temperature Distribution, Thermal Efficiency, and Power Output of a Thermoelectric Element with Variable Properties and Cross Sectional Area." *Advanced Energy Conversion* 2: 219–30.
- Jaziri, N., A. Boughamoura, J. Müller, B. Mezghani, F. Tounsi, and M. Ismail. 2020. "A Comprehensive Review of Thermoelectric Generators: Technologies and Common Applications." *Elsevier: Energy Reports* 6 (Suppl. 7): 264–87.
- Kanimba, E., and Z. Tian. 2016. "Modeling of a Thermoelectric Generator Device." In *Thermoelectric for Power Generation*, Chapter 18, edited by S. Skipidarov, and M. Nikitin, 461–79. Rijeka: IntechOpen. <https://doi.org/10.5772/65741>.
- Kim, N. H. 2010. *Sensitivity Analysis, Encyclopedia of Aerospace Engineering*, Chapter 4, edited by R. Blockley, and W. Shyy, 1–13. West Sussex: John Wiley & Sons.
- Kim, H. S., W. Liu, G. Chen, C. W. Chu, and Z. Ren. 2015. "Relationship Between Thermoelectric Figure of Merit and Energy Conversion Efficiency." *Proceedings of the National Academy of Sciences of the United States of America* 112 (27): 8205–10.
- Kim, M. Y., S. J. Park, G. Y. Kim, S. Y. Choi, and H. Jin. 2021. "Designing Efficient Spin Seebeck Based Thermoelectric Devices via Simultaneous Optimization of Bulk and Interface Properties." *Energy & Environmental Science* 14: 3480–91.
- LeBlanc, S. 2014. "Thermoelectric Generators: Linking Material Properties and Systems Engineering for Waste Heat Recovery Applications." *Journal of Sustainable Materials and Technologies* 1 (2): 26–35.
- Lee, H. 2013. "The Thomson Effect and the Ideal Equation on Thermoelectric Coolers." *Elsevier Energy* 56: 61–9.
- Liu, K., and A. Tovar. 2014. "An Efficient 3D Topology Optimization Code Written in Matlab." *Structural and Multidisciplinary Optimization* 50: 1175–96.
- Macklin, W. J., and P. T. Moseley. 1990. "On the Use of Oxides for Thermoelectric Refrigeration." *Materials Science and Engineering B* 7: 111–7.
- Marlow Industries. 2015. *TG 12-6 Data Sheet*. Also available at <http://onmistytrails.org/wp-content/uploads/2015/03/marlow-industries-inc-tg12-6-00-ba00ddc163.pdf>.
- Mativo, J., and K. Hallinan. 2017. "Development of Compliant Thermoelectric Generators (TEGs) in Aerospace Applications Using Topology Optimization." *Energy Harvesting and Systems* 4 (2): 87–105.
- McCarty, R. 2008. "Engineers Use ANSYS Multiphysics to Study the Mechanical Strength and Thermal Performance of an Innovative Thermoelectric Cooler Design." *ANSYS Advantage* 2 (2): 28–30, <http://www.scribd.com/doc/47154177/ansys-advantage-vol2-issue2>.
- McCarty, R. 2011. *Proprietary Information*.
- Mehta, R. J., Y. Zhang, C. Karthik, B. Singh, R. W. Siegel, T. Borca-Tasciuc, and G. Ramanath. 2012. "A New Class of Doped Nano-Bulk High-Figure-of-Merit Thermoelectrics by Scalable Bottom-Up Assembly." *Nature Materials* 11 (3): 233–40.
- Porter, M. A. 1994. *FEA Step by Step with Algor: Student Edition*. Leawood, Kansas: Dynamic Analysis.
- Poudeu, P. F. P., J. D'Angelo, A. D. Downey, J. L. Short, T. P. Hogan, and M. G. Kanatzidis. 2006. "High Thermoelectric Figure of Merit and Nanostructuring in Bulk P-type $\text{Na}_{1-x}\text{Pb}_m\text{Sb}_y\text{Te}_{m+2}$." *Angewandte Chemie International Edition* 45: 1–5.
- Qu, W., M. Plötner, and W. J. Fischer. 2001. "Microfabrication of Thermoelectric Generators on Flexible Foil Substrates as a Power for Autonomous Microsystems." *Journal of Micromechanics and Microengineering* 11 (2): 146.
- Ragupathi, P., D. Barik, S. Aravind, and G. Vignesh. 2021. "Performance Optimization of Thermoelectric Generators Using Taguchi Method." *IOP Conference Series: Materials Science and Engineering* 1059: 012053.
- Roeser, W. F. 1940. "Thermoelectric Thermometry." *Journal of Applied Physics* 11: 388.
- Rowe, D. M., ed. 2006. *CRC Handbook of Thermoelectric: Macro to Nano*. Boca Raton: RC.
- Rowe, D. M., ed. 2012. *Thermoelectrics and its Energy Harvesting*. Boca Raton, FL: CRC Press.
- Rowe, D. M., and C. M. Bhandari. 1983. *Modern Thermoelectrics*. Reston: Reston Publishing, Inc.
- Ruiz-Ortega, P. E., M. A. Olivares-Robles, and A. F. G. Ruiz. 2018. *Thermoelectric Cooling: The Thomson Effect in Hybrid Two-Stage Thermoelectric Cooler Systems with Different Leg Geometric Shapes, Bringing Thermoelectricity into Reality*. Patricia Aranguren. Rijeka, Croatia: IntechOpen, <https://doi.org/10.5772/intechopen.75440>. Also available at <https://www.intechopen.com/books/bringing-thermoelectricity-into-reality/thermoelectric-cooling-the-thomson-effect-in-hybrid-two-stage-thermoelectric-cooler-systems-with-dif>.
- Sahin, A. Z., and B. S. Yilbas. 2013. "The Thermoelement as Thermoelectric Power Generator: Effect of Leg Geometry on the Efficiency and Power Generation." *Energy Conversion and Management* 65: 26–32.
- Santamaria, J. A., J. Alkorta, and J. Gil Sevillano. 2013. "Mechanical Properties of Bismuth Telluride (Bi_2Te_3) Processed by High Pressure Torsion (HPT)." *Boletín de la Sociedad Española de Cerámica y Vidrio* 52 (3): 137–42.
- Saqr, K. M., and M. N. Musa. 2009. "Critical Review of Thermoelectric in Modern Power Generation Applications." *Thermal Science* 13 (3): 165–74.
- Schmidt, G. R., T. J. Sutliff, and L. A. Dudzinski. 2011. "Radioisotope Power: A Key Technology for Deep Space Exploration." In *Radioisotopes – Applications in Physical Sciences*, edited by Prof. Nirmal Singh, 419–456. Rijeka, Croatia: IntechOpen. Also available at <http://www.intechopen.com/books/radioisotopesapplications-in-physical-sciences/radioisotope-power-a-key-technology-for-deep-space-exploration>.
- Shiozaki, M., T. Toriyama, S. Sugiyama, H. Ueno, and K. Itoigawa. 2004. "Fabrication of Flexible Thermopile Sheet." In *The Fourth International Workshop on Micro and Nanotechnology for Power Generation and Energy Conversion Applications. Power MEMS November 28–30, Kyoto, Japan, 195–8*. Kyoto: Power MEMS.
- Sigmund, O. 2001. "A 99 Line Topology Optimization Code Written in MATLAB." *Structural and Multidisciplinary Optimization* 21 (2): 120–7.
- Sigmund, O. 2007. "On the Design of Compliant Mechanisms Using Topology Optimization." *Journal Mechanics of Structures and Machines* 25 (4): 493–524.
- Sutton, G. W., ed. 1966. *Direct Energy Conversion Vol. 3. Inter University Electronics Series*. New York: McGraw-Hill.
- Telkes, M. 1947. "The Efficiency of Thermoelectric Generators." *International Journal of Applied Physics* 18: 1116–27.

- Telkes, M. 1954. "Solar Thermoelectric Generators." *Journal of Applied Physics* 25 (6): 765–77.
- Thacher, E. F. 1982. "Shapes Which Maximize Thermoelectric Generator Efficiency." In *Proceedings 4th International Conference on Thermoelectric Energy Conversion*, Arlington, Texas, 67–74. New York: Institute of Electrical and Electronics Engineers.
- Tuley, R., and K. Simpson. 2017. "ZT Optimization: An Application Focus." *Materials* 10 (309): 1–8.
- U.S. Patent 6,700,052 B2 issued to Lon E. Bell. 2004. *Flexible Thermoelectric Circuit*. Also available at <http://www.freepatentsonline.com/6700052.pdf>.
- Vijayan, V., and K. Thangavelu. 2012. "Design of Compliant Mechanism for Vibration Isolation Using Topology Optimization and Flexible Building Blocks." *Journal of Engineering and Technology* 3 (1): 46–51.
- Yang, G., R. Niu, L. Sang, X. Liao, D. R. G. Mitchell, N. Ye, J. Pei, J. F. Li, and X. Wang. 2020. "Ultra-High Thermoelectric Performance in Bulk BiSbTe/Amorphous Boron Composites with Nano-Defect Architectures." *Advanced Energy Materials* 10 (41): 2000757.
- Zane, P. J. 2007. *Going with the Flow*. *The News & Observer*. Also available at <http://www.newsobserver.com/lifestyles/sundayjournal/stories/v-print/story/852355.html>.